ACS APPLIED MATERIALS & INTERFACES

www.acsami.org

Research Article

Lattice Strain and Surface Activity of Ternary Nanoalloys under the Propane Oxidation Condition

Haval Kareem, Yazan Maswadeh, Zhi-Peng Wu, Asher C. Leff, Han-Wen Cheng, Shiyao Shan, Shan Wang, Richard Robinson, Dominic Caracciolo, Alex Langrock, David M. Mackie, Dat T. Tran, Valeri Petkov, and Chuan-Jian Zhong*

Cite This: *ACS Appl. Mater. Interfaces* 2022, 14, 11435−11447

Read Online

ACCESS | Metrics & More | Article Recommendations | Supporting Information

ABSTRACT: The ability to harness the catalytic oxidation of hydrocarbons is critical for both clean energy production and air pollutant elimination, which requires a detailed understanding of the dynamic role of the nanophase structure and surface reactivity under the reaction conditions. We report here findings of an in situ/operando study of such details of a ternary nanoalloy under the propane oxidation condition using high-energy synchrotron X-ray diffraction coupled to atomic pair distribution function (HE-XRD/PDF) analysis and diffuse reflectance infrared Fourier transform spectroscopy (DRIFTS). The catalysts are derived by alloying Pt with different combinations of second (Pd) and third (Ni) transition metals, showing a strong dependence of the catalytic activity on the Ni content. The evolution of the phase structure of the nanoalloy is characterized by HE-XRD/PDF probing of the lattice strain, whereas the surface activity is monitored by DRIFTS detection of the surface intermediate formation during the oxidation of propane by oxygen. The results reveal the dominance of the surface intermediate species featuring a lower degree of oxygenation upon the first C−C bond cleavage on the lower-Ni-content nanoalloy and a higher degree of oxygenation upon the second C−C bond cleavage on the higher-Ni-content nanoalloy. The face-centered-cubic-type phase structures of the nanoalloys under the oxidation condition are shown to exhibit Ni-content-dependent changes of lattice strains, featuring the strongest strain with little variation for the higher-Ni-content nanoalloy, in contrast to the weaker strains with oscillatory variation for the lower-Ni-content nanoalloys. This process is also accompanied by oxygenation of the metal components in the nanoalloy, showing a higher degree of oxygenation for the higher-Ni-content nanoalloy. These subtle differences in phase structure and surface activity changes correlate with the Ni-composition-dependent catalytic activity of the nanoalloys, which sheds a fresh light on the correlation between the dynamic change of atomic strains and the surface reactivity and has significant implications for the design of oxidation catalysts with enhanced activities.

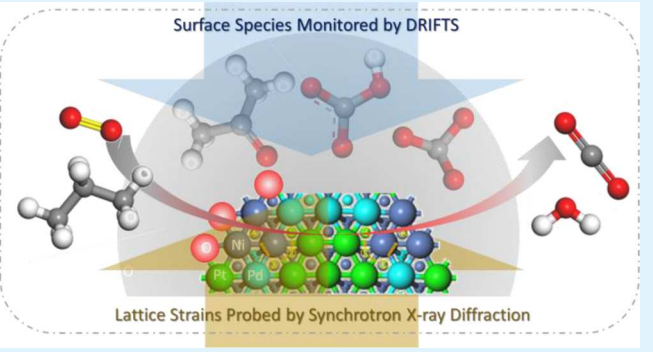

KEYWORDS: *in situ/operando, ternary nanoalloys, synchrotron X-ray diffraction, pair distribution function, diffuse reflectance infrared Fourier transform spectroscopy, propane oxidation, and lattice strain*

1. INTRODUCTION

The development of effective routes for clean energy production and air pollutant elimination involving different hydrocarbons is crucial for energy and environmental sustainability.[1] Among different hydrocarbons, propane is an environmentally friendly fuel[2] since its use exceeds the requirement for clean fuel vehicles,[3−5] and, as the dominant constituent in the commercially available liquefied propane gas (LPG), it has the lowest carbon content of any fossil fuel, minimizing carbon monoxide and greenhouse gas emissions.[6,7] Propane is also nontoxic, noncaustic as the liquid or vapor, cost-effective, and convenient to store and transport.[8,9] Also, it has a high specific energy density (49.6 MJ/kg).[10] The catalytic combustion of light hydrocarbons (C_1 to C_3) is challenging because of the inert nature of their strong C−H bonds and the consequent high-temperature requirement for activation and bond cleavage.[11−14] It is vital to design active, low-cost, and stable oxidation catalysts for overcoming these activation energy barriers. Noble metals and metal oxides have been extensively exploited for oxidation catalysts,[15−19] despite longstanding challenges of catalyst degradation or undesired product formation. For example, the initial high catalytic activity of cobalt oxide was shown to drop

Received: December 12, 2021
Accepted: February 11, 2022
Published: February 23, 2022

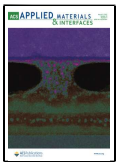

significantly due to the strong interaction between cobalt oxide and support through the Co−O−Al linkage.[20] Another study involves catalytic combustion of C_3 hydrocarbons over Mn_3O_4 where partial oxidation at lower temperature or in a non-oxygen-rich environment results in the emission of toxic hydrocarbons (e.g., aldehydes).[21] Consequently, the development of stable and effective oxidation catalysts is critical for efficient abatement of volatile organic compounds (VOCs). Pt catalysts are widely used in emission control systems but suffer from a propensity to poisoning by CO.[15,22] Rather than simply using more Pt, the combination of noble metals Pt and Pd increases poisoning resistance,[23] showing enhanced catalytic activity for both CO and propane oxidation.[24−26] To further address the high cost of the two noble metals, catalysts that are binary or ternary alloys with Pt, Pd, and non-noble metals have been developed. Some have demonstrated activity and stability superior to Pt and/or Pd and at a low Pt and/or Pd content. In our recent studies,[27−29] alloying Pt or PtPd with a second or third 3d-transition base metal such as Cu, Ni, and Co was shown to create intriguing catalytic synergies for CO oxidation by surface oxyphilicity via the Mars−van Krevelen mechanism[29] and durable oxygen reduction reaction by dealloying−realloying processes.[30] Other examples include a ternary Pt-based catalyst, which showed an enhanced specific activity for alkaline hydrogen evolution reactions by a factor of 10 in comparison with the Pt/C catalyst,[31] and different ternary alloy Pt catalysts for methanol oxidation and oxygen reduction reactions.[32]

Despite such significant progress in developing ternary-based catalysts, understanding of the nanophase and surface structures of the catalysts under the reaction conditions, especially their dynamic details, remains challenging. We report here the employment of a combination of in situ/operando high-energy synchrotron X-ray diffraction coupled to atomic pair distribution function (HE-XRD/PDF)[33−35] and diffuse reflectance infrared Fourier transform spectroscopy (DRIFTS)[34−36] to probe the detailed alloying phase structure and surface intermediate species of ternary PtPdNi nanoalloy catalysts under propane oxidation conditions. The combination of these two techniques for in situ studies of other ternary nanoalloy catalysts in CO and propane oxidation reactions recently revealed intriguing changes in the atomic structure (ordering/disordering) and the reaction mechanism as a result of surface oxygenation under the reaction conditions.[33−35] The HE-XRD/PDF technique examines the nanophase structures of the catalysts, whereas the DRIFTS technique probes the chemical and intermediate species for propane oxidation over the catalysts in correlation with the composition. The dynamic formation of intermediate species over $PdAu/Al_2O_3$ strongly depends on bimetallic composition, which is linked to the catalytic activity in terms of reaction mechanism, selectivity, and achieving a complete C−C cleavage of propane toward CO_2 release.[37,38] In the present work, the nanoalloy catalysts are derived by alloying noble metals (Pt/Pd) with a highly oxyphilic metal (Ni) of various compositions (atomic ratios) which enable the Mars−van Krevelen mechanism for propane oxidation in which the lattice oxygen plays a key role in the oxidation process. A key novelty of this work is the ability to monitor the catalysts' structural evolution and the surface intermediate formation under the reaction conditions by the combined in situ/operando HE-XRD/PDF and DRIFTS techniques, which provides a fresh insight into the role of the catalyst phase structures in the oxidation reaction.

2. EXPERIMENTAL SECTION

2.1. Chemicals. Platinum (II) acetylacetonate ($Pt(acac)_2$, 97%), palladium (II) acetylacetonate ($Pd(acac)_2$, 99%), and nickel (II) acetylacetonate ($Ni(acac)_2$, anhydrous, >95%) were purchased from Alfa Aesar. 1,2-Hexadecanediol (90%), benzyl ether (99%), oleylamine (70%), and oleic acid (99 + %) were purchased from Aldrich. Alumina was purchased from Alfa Aesar. Gases of propane (1 vol % balanced by Ar), H_2 (99.99 vol %), N_2 (99.99 vol %), and O_2 (20 vol % balanced by N_2) were obtained from Airgas. All chemicals were used as received.

2.2. Catalyst Synthesis and Preparation. The general catalyst synthesis and preparation methods have been described in our previous reports.[27,34,36,39] Specifically, in this work, the synthesis of PtPdNi nanoparticles (NPs) involved the reaction of three metal precursors, $Pt^{II}(acac)_2$, $Pd^{II}(acac)_2$, and $Ni^{II}(acac)_2$, in controlled molar ratios in a benzyl ether solvent using oleylamine and oleic acid as capping agents and 1,2-hexadecanediol as a reducing agent. Briefly for the synthesis of PtPdNi, 125 mL of benzyl ether was used to dissolve 1 mmol with a specific feeding ratio of $Pt(acac)_2$, $Pd(acac)_2$, and $Ni(acac)_2$, 5 mmol equally divided between 2.5 mmol oleylamine (OAm) and 2.5 mmol oleic acid (OA) as capping agents, and 2 mmol of 1,2-hexadecanediol as a reducing agent were added into a three-neck flask under vigorous stirring. The solution was heated to between 230 and 260 °C and refluxed for 60 min. PtPdNi NPs with fixed Pt composition (at. 20%) but different Pd and Ni compositions (in atomic ratios, totaling 80%) were produced by controlling feeding molecular ratios of the metal precursors. The NPs were precipitated out and washed by adding ethanol and centrifugation at 3000 rpm for 10 min. The NPs were redispersed in hexane for further use.

For the preparation of Al_2O_3-supported NPs, a typical procedure involved suspending Al_2O_3 in hexane containing a controlled amount of NPs followed by stirring for ∼15 h. The resulting powder was collected and dried under N_2. The supported catalysts were further treated in a quartz tube furnace. The catalyst was first heated at 120 °C in N_2 (nonreactive atmosphere) for 10 min for removing the organic solvent followed by heating at 260 °C in 15 vol % O_2 (oxidative atmosphere) for 30 min for removing organic agents and then at 400 °C under 15% H_2/85% N_2 for 2 h for the catalyst treatment. The effective removal of the capping agents from the NP surfaces by the above calcination and treatment protocol was evidenced by spectroscopic characterizations in our previous studies.[27]

2.3. Catalytic Activity Measurement. To measure the catalytic activity of supported PtPdNi catalysts for the propane (1 vol % balanced by Ar) + O_2 (20 vol % balanced by N_2) reaction, a custom-built system was employed, including a temperature-controlled reactor, gas flow/mixing/injection controllers, and an on-line gas chromatograph (Shimadzu GC 8A) equipped with a 5 Å molecular sieve, Porapak Q packed columns, and a thermal conductivity detector. The catalysts were loaded in a quartz microreactor tube (inner diameter: 4 mm) using quartz wool to fix the catalyst bed in the middle of the tube (length of the catalyst bed: 6 mm). At a flow rate of 20 mL/min, the system was injected with the feeding gas (0.8 vol % propane + 10 vol % O_2 balanced by N_2) through the mounted catalyst in the quartz microreactor. The residence time was about 0.2 s. Gas hourly space velocity (GHSV) in the system is around 16,000 h^{-1}. Temperature control was achieved by a furnace coupled with a temperature controller. The reaction temperature of the catalyst bed was detected by placing a thermocouple probe inside the catalyst bed section. The performance of the catalysts for propane oxidation was determined by the analysis of the composition of the tail gas effusing from the quartz microreactor packed with the catalyst fixed bed using an on-line gas chromatograph.

2.4. Ex Situ Characterizations. Transmission electron microscopy (TEM) was performed using a Hitachi H-7000 electron microscope (100 kV) to determine the particle size and size distribution. High-angle annular dark-field scanning TEM (HAADF-STEM) was employed to determine the morphology of the PtPdNi NPs. HAADF-STEM was performed in JEOL 2100F at 200 kV equipped with an energy-dispersive X-ray spectrometer for elemental mapping distributions. The samples were prepared by dropping a cast of hexane suspension of NPs

https://doi.org/10.1021/acsami.1c24007
ACS Appl. Mater. Interfaces 2022, 14, 11435−11447

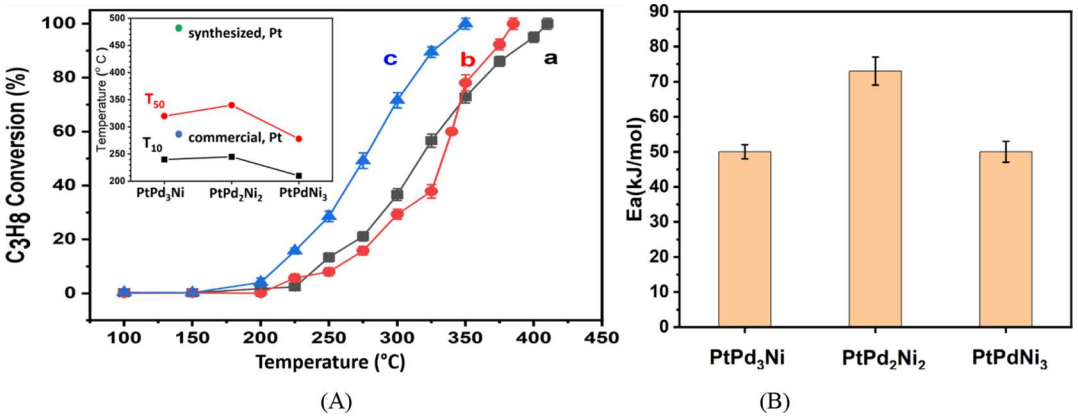

Figure 1. (A) Comparisons of propane conversion activities over the catalysts: $PtPd_3Ni$ (PPN-1) (a, black), $PtPd_2Ni_2$ (PPN-2) (b, red), and $PtPdNi_3$ (PPN-3) (c, blue). Catalyst treatments: as-prepared catalysts (260 °C/O_2 treatment, followed by 400 °C/H_2 treatment). Inset: plots of the reaction temperatures at 10 and 50% conversion, T_{10} and T_{50}, vs the catalyst composition for propane oxidation. (B) Activation energy vs the trimetallic composition.

onto a carbon-coated copper grid, followed by solvent evaporation at room temperature. Inductively coupled plasma-optical emission spectroscopy (ICP-OES) was used to analyze the composition, which was performed using a Perkin−Elmer 2000 DV ICP-OES utilizing a cross-flow nebulizer with the following parameters: plasma 18.0 L $Ar_{(g)}$/min; auxiliary 0.3 L $Ar_{(g)}$/min; nebulizer 0.73 L $Ar_{(g)}$/min; power 1500 W; peristaltic pump rate 1.40 mL/min. Elements <1.0 mg/L were analyzed using a Meinhardt nebulizer coupled to a cyclonic spray chamber to increase analyte sensitivity with the following parameters: 18.0 L $Ar_{(g)}$/min; auxiliary 0.3 L $Ar_{(g)}$/min; nebulizer 0.63 L $Ar_{(g)}$/min; power 1500 W; peristaltic pump rate 1.00 mL/min. Laboratory standards were analyzed every 6 or 12 samples, with instrument re-calibration if the standards were not within ±5%. Thermogravimetric analysis (TGA) was performed on a Perkin−Elmer Pyris 1-TGA for determining the metal loadings.

2.5. In Situ/Operando Characterizations. Combined in situ/operando DRIFTS and total X-ray scattering experiments were carried out using the DRIAD-X reaction cell at the beamline 11-ID-B at the Advanced Photon Source, Argonne.[40] The design of the cell ensures that the infrared and X-ray beams probed coinciding sample volumes. In particular, diffuse DRIFTS data were acquired on a Bruker Vertex 80 FTIR spectrometer with a MCT detector and a Praying Mantis Diffuse Reflectance Accessory (Harrick Scientific Products, Inc.). Briefly, the sample cup in Praying Mantis Diffuse Reflectance Accessory was filled up with 30 mg of the catalyst over which the propane oxidation reaction was carried out at a controlled temperature (e.g., 270 °C). The spectra were collected by averaging 64 scans with a resolution of 2 cm^{-1}. Concurrently, XRD data were taken using X-rays with an energy of 86.70 keV (λ = 0.1429 Å) and a large-area detector. Experimental XRD data were corrected for experimental artifacts, reduced to the so-called structure factors, $S(q)$, and then Fourier-transformed to atomic PDFs $G(r)$ using a wave vector defined as $q = 4\pi\sin(\theta)/\lambda$, where θ is half of the scattering (Bragg) angle and λ is the wavelength of X-rays used. In the present experiments, XRD data were collected up to wave vectors q_{max} of 30 Å. Note that atomic PDFs $G(r)$ are experimental quantities that oscillate around zero and show positive peaks at real space distances, r, where the local atomic density $\rho(r)$ exceeds the average atomic density ρ_o. This behavior can be expressed by the eq $G(r) = 4\pi r\rho_o[\rho(r)/\rho_o - 1]$, which is the formal definition of the PDF $G(r)$.

2.6. Computational Modeling. Ab initio calculations were conducted by density functional theory (DFT) with the DMol[3] program coming as a part of Materials Studio program. In the computation, the generalized gradient approximation (GGA) and the Perdew−Burke−Ernzerhof (PBE) functional were used. A double-numerical basis set with polarization functions was used in all theoretical calculations. A three-layer periodical surface slab model with a 3 × 3 unit cell was built in consideration of the ternary alloy composition. The bottom two layers were fixed, while the top layer was allowed for relaxation. Various elements were exposed on the surface to study the binding strength of each metallic element with O species. The binding energies of O species at different surface sites on the model were evaluated after full geometry optimizations. The transition states on the model were located and optimized for the oxygen atom diffusion elementary steps, with only one imaginary frequency. The diffusion barrier (ΔE_a) of the oxygen atom on the alloy model was calculated by $\Delta E_a = E_{TS} - E_{IS}$, where E_{TS} and E_{IS} denote the energies of the transition state and the reactant, respectively.

3. RESULTS AND DISCUSSION

3.1. Morphology and Composition. The composition of metals in the ternary NPs was controlled by keeping the feeding ratio of Pt constant at 20 at % while changing the Pd and Ni feeding ratios in the synthesis solution (Pd + Ni total 80 at %). ICP-OES was used to determine the actual composition in the resulting ternary NPs. The linear relationship between Pd % in the NPs and Pd % in the synthesis feeding (Figure S1) indicates a good controllability over the composition of the trimetallic catalyst. Among different compositions, NPs with three different atomic ratios, $PtPd_3Ni$ (PPN-NP1), $PtPd_2Ni_2$ (PPN-NP2), and $PtPdNi_3$ (PPN-NP3), with an average size of 5.8 ± 1.7, 5.6 ± 2.2, and 7.7 ± 2.9 nm (± standard deviation), respectively, were synthesized in this study. The actual compositions determined by the ICP-MS method are 18% Pt, 63% Pd, and 19% Ni for PPN-NP1; 17% Pt, 42% Pd, and 41% Ni for PPN-NP2; and 16% Pt, 16% Pd, and 68% Ni for PPN-NP3. The wet-chemical synthesis of the NPs enabled a better control over the size in comparison with the traditional synthesis methods such as impregnation, co-precipitation, or deposition−precipitation. The NPs were supported on alpha-Al_2O_3 powders by a standard dispersion procedure.[41] Alpha-Al_2O_3 is a support with a high surface area[41] and high thermal stability. This support also features strong interaction with noble metals.[42] The supported NPs were then thermochemically treated by the standard thermochemical parameters as described in the Experimental Section, which allowed effective removal of the capping agent as shown in our previous study.[43] The NPs, after loading on the support and undergoing thermochemical treatment, are mostly well dispersed (Figure S2A−C). The average size of the NPs is 9.5 ± 3.2, 6.2 ± 1.9, and 10.5 ± 4.6 nm for $PtPd_3Ni$ (PPN-NP1)/Al_2O_3, $PtPd_2Ni_2$ (PPN-NP2)/Al_2O_3, and $PtPdNi_3$ (PPN-NP3)/Al_2O_3 (Figures S1 and S2), which are named as PPN-1, PPN-2, and PPN-3, respectively, in this report. The

https://doi.org/10.1021/acsami.1c24007
ACS Appl. Mater. Interfaces 2022, 14, 11435−11447

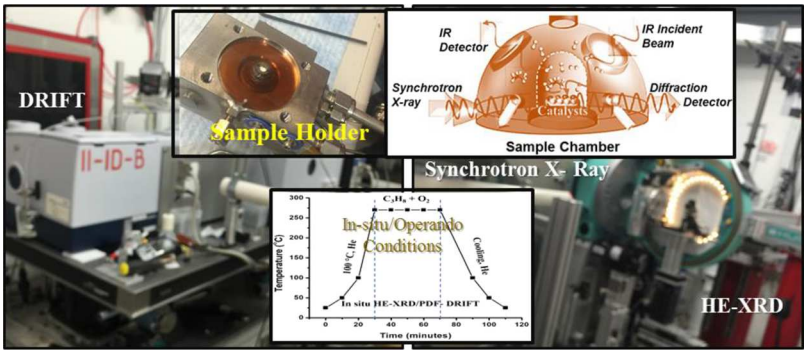

Figure 2. Photo of the in situ/operando HE-XRD and DRIFTS measurement setup in the synchrotron X-ray facility. The reaction conditions in terms of the temperature and gas flow are also illustrated in the inset.

ternary composition distributions were also determined by HAADF-STEM images and the corresponding energy-dispersive X-ray spectroscopy (EDX) elemental mapping for the supported PtPdNi NPs (Figure S2 bottom panel). The mapping data show largely uniform distributions of the three metals across the NPs. This feature is characteristic of a random alloy with little indication of phase segregation for most of the NPs observed in the mapping images. As shown by EDX line profiles (Figure S3), the element distributions are relatively uniform across the NPs, though subtle local variations were observed, which reflected a certain degree of heterogeneity due to segregation of small phase domains in the NPs. The heterogeneity could arise from the subsequent thermochemical treatment to remove the capping agents since the as-synthesized ternary NPs were relatively homogeneous.[30] The uniform ternary composition is also supported by examination of the crystalline features of the NPs. An example is shown by the analysis of the lattice fringes in the HRTEM image of PPN-2, yielding 0.2335 nm (see Figure S4), which is consistent with the alloy's characteristic d(111) spacing.[44]

3.2. Catalytic Activity. The measurement of the catalytic activity for propane oxidation was focused on PtPdNi/Al_2O_3 of three different compositions. Figure 1A shows a representative set of catalytic conversion data for the as-prepared catalysts (260 °C/O_2 treatment, followed by 400 °C/H_2 treatment). Based on the reaction temperature, the catalytic activity over the PtPdNi/Al_2O_3 catalyst is shown to increase in the following trend: PPN-3 > PPN-2 > PPN-1. Clearly, the relative composition of Ni played an important role in the catalytic activity, showing the highest activity for the catalyst with the highest Ni composition ($PtPdNi_3$), that is, PPN-3. This activity is also found to be higher than that for propane oxidation over the $Pt_{22}Pd_{78}/Al_2O_3$ catalyst (see Figure S5). This finding is remarkable because it suggests an important role of oxophilicity of the alloyed metal component on catalytic activity for hydrocarbon oxidation. As shown by the plots of the reaction temperatures for T_{10} and T_{50} vs the trimetallic composition for propane oxidation (Figure 1A inset), the reaction temperature shows a maximum value at a composition of ~50% Ni. Both T_{50} and T_{10} values were the lowest for the catalyst with the highest Ni composition. For example, for $PtPdNi_3$ (PPN-3), T_{50} = 278 °C, which is lower in comparison with those reported for monometallic Pd/Al_2O_3 (T_{50} = 390 °C),[45] Pt/Al_2O_3 (T_{50} = 350 °C),[46] and $PtPd_4/Al_2O_3$ (T_{50} = 321 °C) (see Figure S5).

The overall activation energies (E_a) of propane oxidation (Figure S6) are smaller than those reported for the catalytic oxidation of propane (60−90 kJ/mol).[21] The E_a for PPN-3 exhibited the smallest value (39 kJ/mol), whereas the E_a for PPN-2 (52 kJ/mol) is the highest (Figure 1B). This finding is consistent with the trends of T_{50} and T_{10} values (Figure 1A inset). The catalytic activity over PPN-2 is lower than that of PPN-1 in terms of T_{50} and T_{10}, which is consistent with the higher activation energy for PPN-2. Note that these catalysts feature the different compositions in atomic ratios and the same metal loading (5% wt) on Al_2O_3 and similar size of particles (8∼11 nm). It is evident that the composition of the NPs is the main factor contributing to the difference in the catalytic performance under the reaction condition. This is consistent with a previous study, where the addition of nickel to ruthenium increased the propane reforming rate by the reduction of activation energies.[7]

3.3. In Situ/Operando HE-XRD/PDF and DRIFTS Characterizations. To gain an in-depth understanding of the reaction mechanism and surface intermediate species during the reaction condition, we carried out detailed in situ studies of these ternary catalysts with different compositions using HE-XRD coupled to element-specific atomic PDF and DRIFTS techniques to probe the NP phase structure evolution and surface species formation under real-time reaction conditions of propane oxidation (Figure 2). The data are analyzed in terms of the atomic phase structure, the lattice parameter, the intermediate species, and the surface-active sites.

3.3.1. In Situ HE-XRD/PDF. The synchrotron X-ray HE-XRD coupled with PDF was used to examine the atomic-scale alloying phase structure. Figure 3 shows a set of in situ PDFs of the three Al_2O_3-supported PtPdNi catalysts at three different stages of the in situ experiments. It starts from room temperature for the fresh catalyst, being treated first in He at 100 °C for 30 min, then propane oxidation under the reaction condition (propane + O_2) at 270 °C, and then cooling under He. The presence of the sharp peaks in the atomic PDF is a characteristic of well-defined atomic coordination spheres in terms of the atomic-scale structures. The sharp peaks are reflections of pairs of atoms, nearest, immediate, and farther neighbors within the NPs at each radial distance. In the right column (A′, B′, and C′), 3D PDF color maps are derived from the in situ data set reflecting the intensity changes as a function of time, along with a projection over the XY plane (bottom map) to guide the eye through the atomic fluctuations.

In order to extract the structural information from the PDF data, PDF fit was carried out using a calculated PDF derived from a theoretical crystallographic model. The atomic arrangement fits well with the face-centered-cubic (FCC) alloy structure. For the changes in the atomic distances and

https://doi.org/10.1021/acsami.1c24007
ACS Appl. Mater. Interfaces 2022, 14, 11435−11447

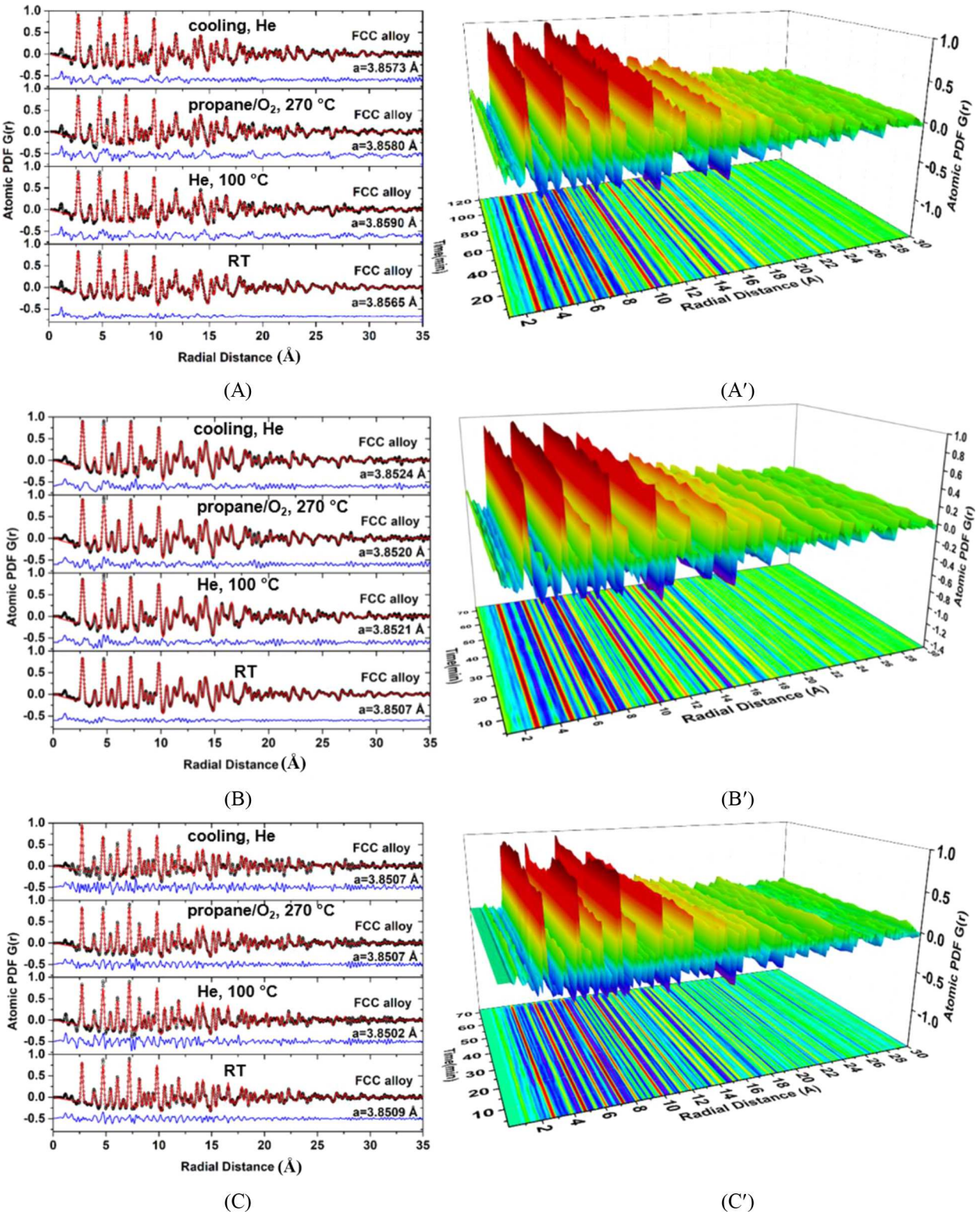

Figure 3. In situ PDFs for (A) $PtPd_3Ni$ (PPN-1), (B) $PtPd_2Ni_2$ (PPN-2), and (C) $PtPdNi_3$ (PPN-3) catalysts. In the left column: selected atomic PDFs at four stages, starting from the fresh catalyst under room temperature (RT), heating under He at 100 °C, propane/O_2 reaction at 270 °C, and then cooling under He. Experimental PDF data (symbols in black), PDF fit based on the theoretical model (line in red), and difference line between the experimental and calculated PDFs (line in blue). The PDF is well approximated with a model (red line) based on an FCC-type structure for the alloy NPs. In the right column: (A′, B′, and C′) 3D PDF color map derived from the in situ data set with a projection over the *XY* plane (bottom map) to guide the eye through the atomic fluctuations.

arrangement of data for catalysts with different treatment or reaction conditions, the difference line (the line in blue underneath the PDF curve in Figure 3A−C) is a good indicator about the goodness of the fit. As shown by the first PDF data for the beginning of the treatment or reaction condition, the NPs match with the random FCC alloy structure (the blue line with

https://doi.org/10.1021/acsami.1c24007
ACS Appl. Mater. Interfaces 2022, 14, 11435−11447

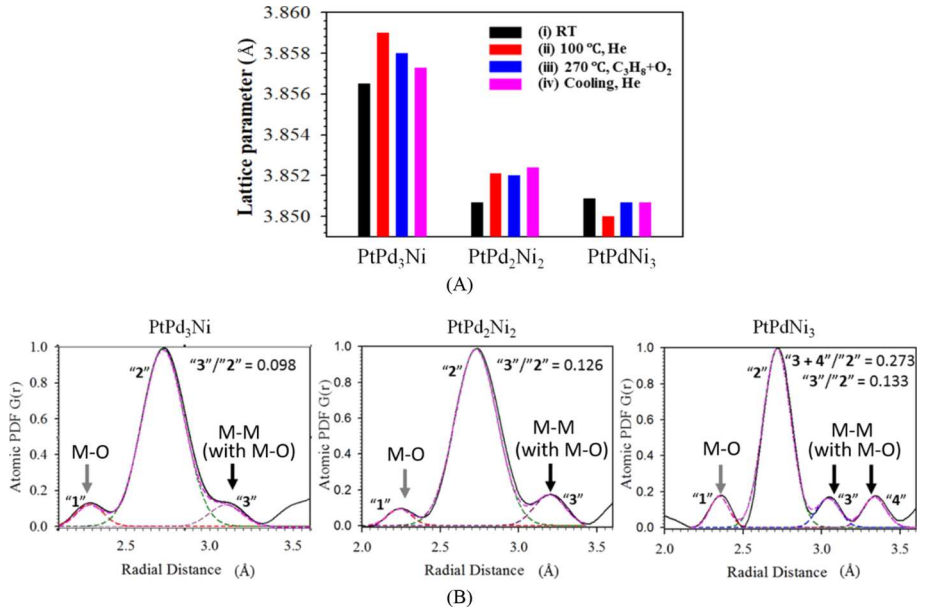

Figure 4. (A) Plots of FCC-lattice parameter catalyst composition at the different stages, including the fresh catalyst at room temperature (RT, i), treatment in He at 100 °C (ii), oxidation of propane/O_2 at 270 °C (iii), and cooling in He (iv). (B) Analysis of the PDF patterns in the low-r (∼2.7 Å) region (Figure S7) for $PtPd_3Ni$ (PPN-1), $PtPd_2Ni_2$ (PPN-2), and $PtPdNi_3$ (PPN-3) during the propane oxidation reaction. The snapshot PDF (black line) is deconvoluted into three to four PDF peaks (dashed lines from left to right: 1, 2, 3, and 4), revealing M−O species (mainly Ni−O) and M−M bond distances associated with the M−O species, and their intensity ratios to the 2.72 Å peak.

less fluctuations). Although the presence of some small degree of heterogeneity in the NPs could affect the PDF peak width, it may not have a significant impact on the lattice parameter since it was extracted from fitting the PDF curves as an average. We have also included EDX line profiles in the Supporting Information (Figure S3), showing that the element distributions are relatively uniform across the NPs. We believe that the overall trend of the average lattice parameters obtained in this work should remain unchanged. The NP structure shows deviation from the FCC crystallographic model during the reaction (as shown by the increased fluctuations in the blue line). Under the reaction condition, the oxygen activation, oxygenation, and carbon reaction occur on the surface of the NPs that changes the surface structure and induces stress/strain to the atomic structure. Nevertheless, the majority of the atoms preserve their position at the random FCC structure, showing less symmetry compared to the theoretical FCC model. The atomic arrangement largely maintains the FCC alloy structure throughout the sequences of treatment and reaction. The PDF is well approximated with a nanoalloy model (red line) based on an FCC-type structure (Figure 3A−C). Upon increasing the temperature and the exposure to the oxidation reaction condition, the NPs are shown to display atomic disordering that broke the crystal periodic symmetry at the high radial distance, leading to a noticeable noise signal in the radial region after 30 Å (Figure 3A−C).

The nanoalloy phase structures and the lattice parameters of $PtPdNi/Al_2O_3$ catalysts can be extracted from the analysis of the experimental PDF data. For the fresh catalysts, the lattice constants are 3.8565, 3.8507, and 3.8509 Å for $PtPd_3Ni$, $PtPd_2Ni_2$, and $PtPdNi_3$ catalysts, respectively. In comparison with the lattice parameters for Ni (3.499 Å), Pt (3.912 Å), and Pd (3.859 Å),[47] the subtle differences reflect the nanoalloy characteristics. As shown in Figure 4A, the FCC-lattice parameters for both PPN-1 and PPN-2 showed an increase upon elevating the temperature from room temperature (i) to 100 °C under He (ii) and a slight decrease upon exposure to propane/O_2 at 270 °C (iii). PPN-1 showed a further decrease upon cooling down to room temperature in He (iv), whereas PPN-2 showed almost no more change. Interestingly, the FCC-lattice parameter for the PPN-3 catalyst showed a decrease in He at 100 °C (ii) and then a slight increase under propane/O_2 at 270 °C. Overall, the lattice parameter remained the lowest for the PPN-3 catalyst among the three catalysts.

In view of the important role of surface oxygenation in the catalytic oxidation reaction, we further examined the in situ PDF patterns in the low-r (∼2.7 Å) region (Figure S7) in detail. As shown in Figure 4B by atomic PDF peaks and peak deconvolution around a radial distance of ∼2.72 Å upon exposing the catalyst to the oxidation reaction condition, there are two small peaks, one at 2.3∼2.4 Å and the other at 3.2∼3.4 Å. This indicates the presence of well-structured metallic oxide layers on the nanoalloy, likely reflecting cubic NiO or tetragonal PtO/PdO phases.[37] The peak at ∼2.3 Å reflects the presence of cubic NiO, whereas the peak at ∼3.2 Å indicates the presence of metal−metal (Pt/Pd) bonding as a result of the formation of the NiO species in the lattice. There is a subtle increase for the relative peak ratio of ∼3.1 Å to the 2.7 Å peak as Ni% is increased in the ternary NPs, as indicated in Figure 4B. Interestingly, the peak at ∼3.1 Å is apparently split into two peaks for PPN-3, which likely reflects a higher degree of NiO formation. Note that the intensity for the peak characteristic of the metal−oxygen bond in the experimental PDFs during the propane oxidation reaction is small, likely because the amount of Pt/Pd on the surface of the catalyst is relatively small. A similar signal was obtained during the CO oxidation reaction over different catalysts in our previous study.[37] For $PtPd_3Ni$ (PPN-1), $PtPd_2Ni_2$ (PPN-2), and $PtPdNi_3$ (PPN-3), the average surface bonding distance is 2.72 Å under the oxidation conditions, showing disordering at the atomic level. The oxidation condition involves both surface and lattice oxygenation and leads to the appearance of metal-to-metal atom distances, attributed to the presence of the metal−oxygen species in the structure.[36] In the

https://doi.org/10.1021/acsami.1c24007
ACS Appl. Mater. Interfaces 2022, 14, 11435−11447

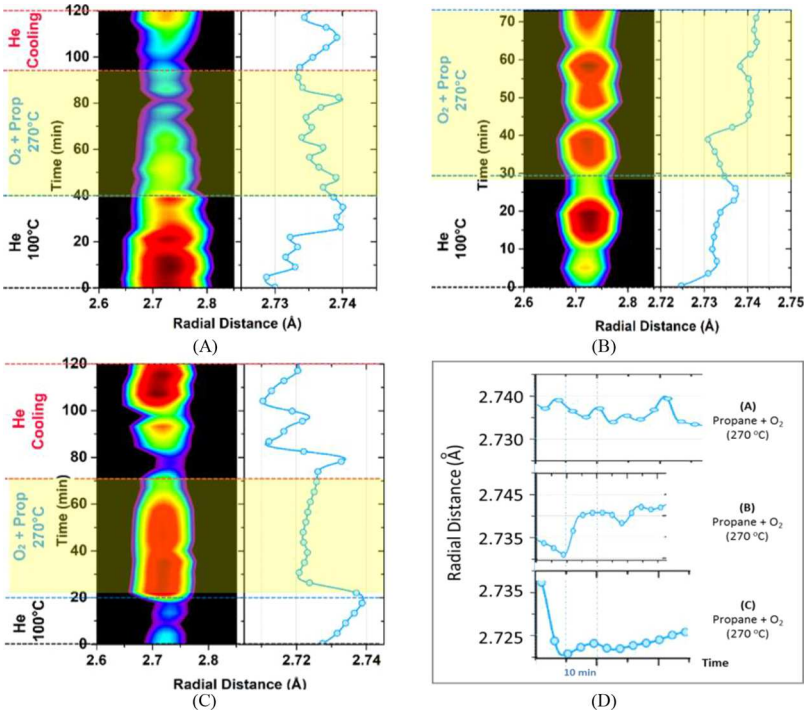

Figure 5. Comparisons of the in situ atomic PDFs for $PtPdNi/Al_2O_3$ exposed to different stages of the reaction: heating in He at 100 °C, propane oxidation at 270 °C, and cooling in He for (A) $PtPd_3Ni$ (PPN-1), (B) $PtPd_2Ni_2$ (PPN-2), and (C) $PtPdNi_3$ (PPN-3). Left panel: the reaction conditions (gas atmosphere, temperature, and reaction time); middle panel: color map of the PDF peak intensity at the radial distance of ∼2.7 Å and the oscillation vs time, where the intensity increase is represented by the color change from purple to dark red. Right panel: plot of the first PDF peak position (interatomic distance) vs time. The yellow highlighted region represents the reaction region. (D) Comparison of the changes in the reaction region.

case of PtPdNi, the low-r PDF pattern is characteristic of the cubic-like NiO and/or tetragonal-like Pt/Pd−O species in the disordered structure, as reflected by a mixture of FCC-type packed metal atoms and the oxidized metal species (e.g., Ni−O/Pt−O). The degree of surface/lattice oxygenation shows an increase in the order of PPN-1 ≤ PPN-2 < PPN-3, which apparently correlates well with the order of the catalytic activity for the three catalysts (PPN-1 ≈ PPN-2 < PPN-3). The presence of Ni in the alloy is thus believed to have played an important role in providing an active site for the oxygenation reaction in the propane oxidation process. As shown in Figure S7, the peaks, which are already present in the fresh catalysts with different intensities, show highly dynamic M−M features associated with the metal oxygenation species or oxides. At this point, we are not able to pin down the specific Pt−Pt or Pd−Pd features because the peak intensities are weak. However, there are subtle differences among the fresh PPN-1, PPN-2, and PPN-3 catalysts (Figure S7A−C). Further studies are needed to correlate these peaks quantitatively with the presence of the surface oxygenated metal species.

An analysis of the atomic bonding distances from the in situ data indicated that the nanophase structures experienced different degrees of reconstruction depending on the bimetallic composition. As shown in Figure 5, fluctuations or irregular oscillations of small atomic stress/strain occur upon increasing the temperature under He, exposing to propane and oxygen at 270 °C, and cooling down under He (Figure 5A−C). Remarkably, the overall fluctuations or irregular oscillations in the bonding distances characteristic of the ternary nanoalloys depend not only on the catalyst composition but also on the reaction atmosphere and temperature. Under propane and oxygen at 270 °C, the average atomic bond distance (near-atomic neighbor) fluctuates between 2.732 and 2.740 Å for PPN-1 (Figure 5A) and 2.730 and 2.742 Å for PPN-2 (Figure 5B). PPN-3 showed a drastic decrease from 2.737 to 2.720 Å in the first 10 min, which was followed by a small and steady increase into 2.725 Å in the remaining reaction period (Figure 5C). Figure 5D shows these subtle differences of the atomic bond fluctuations in the entire propane oxidation reaction period. The fluctuations in the local atomic arrangement are clearly shown by the color-coded PDF patterns where the intensity of the atomic PDF peak (z-axis) is represented by different colors' spreading over most of the peak width. Note that not only the peak intensity but also the center of the peak varies with time, reflecting the oscillatory characteristic for the metal−metal bonds in the NPs under the surface reaction condition. We also note that there is a possibility for the existence of amorphous metal oxides which could mainly impact the peak widths and intensities. The HE-XRD and PDF patterns did not reveal any obvious phase segregation, and they can be fit well with the FCC model. The HR-TEM data also support the FCC characteristic for the NPs. Note that the current results do not rule out the presence of some amorphous oxide species on the surface, which will be studied in future imaging and modeling studies.

Among the three catalysts, the more active catalyst involves more surface activities in terms of binding/breaking atomic bonds under the reaction condition. The difference between the local atomic structure and the average atomic structure of the NPs is reflected by the subtle fluctuation in local order (Figure 5). The change of the first interatomic distance (bonding distance) on the NP surface is dynamic. The surface/subsurface

https://doi.org/10.1021/acsami.1c24007
ACS Appl. Mater. Interfaces 2022, 14, 11435−11447

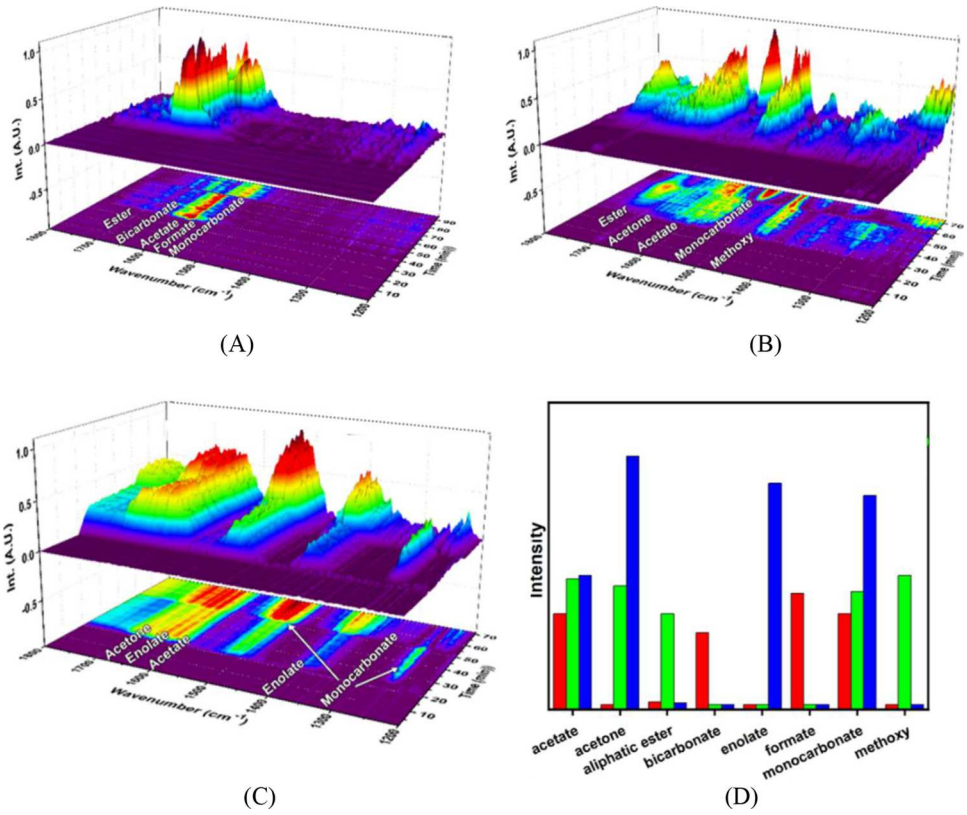

Figure 6. 3D map plots of the in situ DRIFTS spectra recorded during propane oxidation over $PtPd_3Ni$ (PPN-1) (A), $PtPd_2Ni_2$ (PPN-2) (B), and $PtPdNi_3$ (PPN-3) (C) catalysts at 275 °C in the 1800−1200 cm^{-1} region. Under each 3D map, the corresponding 2D map plot is included along with the IR band assignments (see also the DRIFTS spectra in Figure S8). (D) Comparison of the changes in the reaction region of the DRIFTS peak intensities for some of the major intermediate species detected in propane oxidation at 270 °C over PPN-1 (red bars), PPN-2 (green bars), and PPN-3 (blue bars) catalysts. The intermediate species are arranged from the noncleaved or first C−C bond cleaved oxidation species (acetone, ester, and acetate) to complete the C−C bond cleaved oxidation species (formate and bicarbonate).

oxygenation and deoxygenation is also partially reflected by the asymmetric character of the peak intensity distribution. Indeed, a certain degree of irregular interatomic bonding distance oscillations is observable in the three-surface treatment/reaction stages in terms of the peak center position (the curves in the right panels in Figure 5A−C). The changes in the peak position for the three catalysts partially reflect the differences in the variation of the nearest-neighbor interatomic distances under the reaction condition.

The surface of the ternary nanoalloy catalysts may undergo stress/strain during the reaction, which could lead to the atomic bond fluctuation. It is likely that the surface/subsurface oxygenation and deoxygenation of the Ni species in the nanoalloy contribute to the strain fluctuation from the beginning of the reaction. The temperature also influences the changes in the interatomic lattice strain. It is interesting to observe that the PPN-3 catalyst shows a large change in the interatomic bond distances ranging between 2.71 and 2.74 Å (0.03 Å, ∼1.1%) during the reaction. The atomic strain occurs upon increasing the temperature to 100 °C (the first 20 min). This is followed by a sudden drop of the average atomic bond distance upon introducing propane and oxygen, that is, the propane oxidation reaction condition, which is apparently linked to the formation and breaking of the metal−oxygen bonds on the catalyst surface. Moreover, the atomic bond fluctuations appear very small for PPN-3 (Figure 5D). For the other two catalysts (Figure 5A,B), greater oscillatory changes are observed in terms of the average atomic bond distance, showing 2.725−2.743 Å (0.02 Å, ∼0.6%) for PPN-2 and 2.73−2.74 Å (0.01 Å, ∼0.4%) for PPN-1. It is important to note that PPN-3 NPs feature a higher percentage of Ni atoms in the nanoalloy than the other two NP catalysts. This catalyst showed the highest activity and stability (see Figure 1). The high activity of PPN-3 NPs may be attributed to the fact that the bonding distance went under significant stress and the stress led to optimization of the Fermi level in comparison to the d-bond, thus reducing the adsorption energy and facilitating the oxidation of the carbonaceous species into CO_2. In our previous study of ternary PtAuNi catalysts, the catalyst with a higher percentage of Ni was shown to be more stable than NPs with less Ni.[37] While the detailed mechanism for the oscillatory changes is not clear at this point, these findings suggest a possible connection between the interatomic distances in the NPs and the surface activity, for which we further examined the data from the DRIFTS as described next.

3.3.2. In Situ DRIFTS. Given the observation of the changes of the interatomic distances during the catalytic propane oxidation over $PtPdNi/Al_2O_3$ catalysts in the in situ PDF data, we further probed the surface species during propane oxidation by in situ DRIFTS. This study is directed to gain an insight into the correlation among the nanostructure, the surface sites, and the catalytic activity. Figure 6A−C (and Figure S8) presents a typical set of DRIFTS spectra monitoring the surface intermediate species during propane oxidation over $PtPdNi/Al_2O_3$ catalysts of different compositions. Under each of the 3D maps in Figure 6A−C, the corresponding 2D map plot is included, showing the assignments of the IR bands. There are

https://doi.org/10.1021/acsami.1c24007
ACS Appl. Mater. Interfaces 2022, 14, 11435−11447

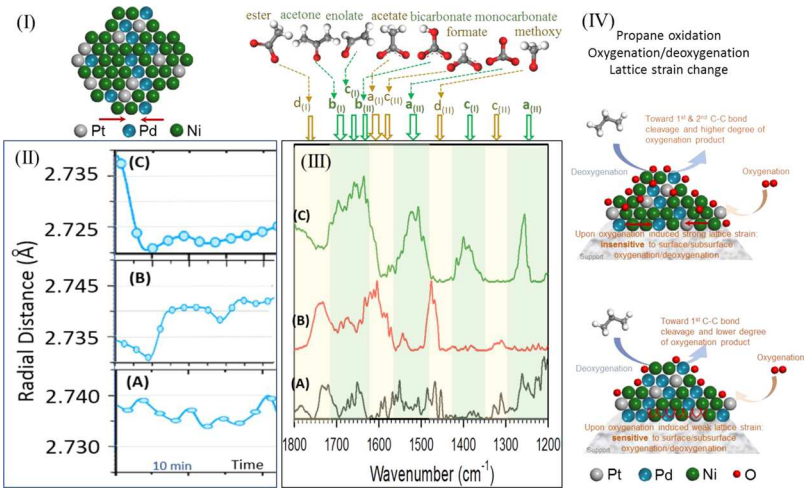

Figure 7. (I) Illustration of surface species of the propane oxidation and interatomic lattice of the oxygenated ternary PtPdNi NPs; (II,III) comparisons of snapshots of in situ PDF peak positions in terms of the average bond distances (II) and DRIFTS peak positions (III) in terms of the surface species (top panel) for PPN-1 (A), PPN-2 (B), and PPN-3 (C) (note that the intensities of B and C were scaled up by a factor (2∼5) for a better visual comparison). (IV) Illustrations of the proposed surface oxygenation/deoxygenation and lattice strain change for propane oxidation over low-Ni (bottom) and high-Ni (top) catalysts.

clearly subtle differences in terms of the surface intermediate species, which are highly dependent on the composition of the ternary catalysts.

The position and intensity of the observed peaks (Figure S8) depend on the composition of the catalyst. In the range (2850−3000 cm^{-1}), the observed bands correspond to C−H vibration bonds of gaseous propane, CH_2 (ads), and CH_3 (ads) species.[48] The observed bands in 2340−2360 cm^{-1} are characteristic of gaseous CO_2.[20] Major peaks in the range of 1730−1330 cm^{-1} are characteristic of intermediate species evolved during propane oxidation. The evolution of oxy-carbon bands is examined in detail in the range of 1800−1200 cm^1 (Figure 6 and Figure S9). As the reaction progresses, the intensities of the bands become stronger for PPN-1 (Figure 6A), PPN-2 (Figure 6B) and PPN-3 (Figure 6C). The peaks at 1590−1607 (Figure 6B) and 1578 cm^{-1} (Figure 6C) are assigned to the adsorbed acetate ν_{as} (COO) species.[46,49,50] The peaks from 1681 to 1714 cm^{-1} (Figure 6C) and 1672 cm^{-1} (Figure 6B) can be assigned to the acetone ν (C═O) stretching mode.[51] The bands at 1737 cm^{-1} (Figure 6B) and 1720−1730 cm^{-1} (Figure 6A) are likely due to the absorption of the carbonyl group with the aliphatic ester function υ (C═O).[52,53] The band at 1650 cm^{-1} (Figure 6A) is in agreement with the bicarbonate ν_{as} (OCO^-) species stretching bond.[54,55] The enolate species (CH_2═CH−O) exhibit bands at 1636, 1653, and 1400 cm^{-1} (Figure 6C).[56,57] The band at 1591 cm^{-1} is consistent with the absorption of the formate ν_{as} (COO) species (Figure 6A). The peaks at 1464 (Figure 6A) and 1470 cm^{-1} (Figure 6B) are attributed to the adsorbed methoxy δ_{as} (CH_3) groups.[58,59] The bands at 1500, 1532, and 1256 cm^{-1} (Figure 6C), 1544 (Figure 6B), and 1549 cm^{-1} (Figure 6A) are most likely attributed to ν_{as} (COO) and ν_s (OCO) monodentate carbonate species.[48] A close examination of the peaks for PPN-1 and PPN-2 (Figure 6A,B) shows aliphatic ester at 1720−1737 cm^{-1} and methoxy at 1470 cm^{-1}, which are absent for PPN-3. The data shows the emergence of bicarbonate 1653 cm^{-1} and formate at 1591 cm^{-1} only for PPN-1. Moreover, the species of acetate at 1580 and 1578 cm^{-1}, acetone at 1681 to 1714 cm^{-1} and 1672 cm^{-1}, and enolate at 1636, 1653, and 1400 cm^{-1} were detected over PPN-3 and PPN-2 but were not detected over PPN-1. This result shows that the growth of oxy-carbon species (COO, OCO, CCO, etc.) during the oxidation reaction is correlated with the bimetallic composition, suggesting different reaction pathways of propane oxidation.

In Figure 6D, the peak intensities of oxy-carbo species in the range of 1200−1800 cm^{-1} are further compared. Peaks for acetate, acetone, enolate, and monodentate carbonate species are maximized over PPN-3, whereas the aliphatic ester and methoxy species are maximized over PPN-2. Bicarbonate and formate species are maximized over PPN-1. These detections of the different surface species indicate that the formation of the surface intermediate species strongly depend on the trimetallic composition of the catalysts. Note that our on-line GC system was configured to determine the CO_2 product in this study. The product was confirmed by the carbon balance calculation based on the CO_2 peak. While the in situ DRIFT data (Figures 6 and S8 and Table S1) did detect different intermediate species, the analysis of the gas product selectivity in correlation with the surface intermediate species will be part of our future studies.

3.3.3. Correlation between the Lattice Changes and the Surface Activities. Taken together, the results from the in situ HE-XRD/PDF and DRIFTS characterizations have provided some intriguing insights into the correlation between the growth of surface carbonaceous species and the changes in atomic structures during the catalytic oxidation of propane. To assess the relative changes of the surface species and the interatomic lattice of the oxygenated ternary NPs (Figure 7I), we further compared the in situ PDF peak positions in terms of the average bond distances (Figure 7II) and the DRIFTS peak positions (Figure 7III) in terms of the surface species for $PtPd_3Ni$ (PPN-1), $PtPd_2Ni_2$ (PPN-2), and $PtPdNi_3$ (PPN-3). During propane oxidation, the dynamic change of interatomic distances is evidenced by the PDF data, whereas the formation of carbonaceous species is indicated by the DRIFTS data. Upon exposing to propane/O_2, the average atomic bond distance for PPN-3 shows an abrupt decrease, reflecting the absorption of oxygen or carbonaceous species. The amplitude of this change is much smaller for PPN-1 and PPN-2. However, in comparison with the relatively constant value for PPN-3 after the decrease (Figure 7IIC), PPN-1 and PPN-2 show subtle oscillatory

https://doi.org/10.1021/acsami.1c24007
ACS Appl. Mater. Interfaces 2022, 14, 11435−11447

changes (Figure 7 (II) A,B). The reactivity of the surface/lattice oxygen and the consequent change in lattice strain in the NPs may have played a role in the above differences. This is further assessed by analyzing the surface intermediate species during propane oxidation (Figure 7III). The assignments of the peak positions to the intermediate species are illustrated on the top panel of Figure 7III, the details of which are given in Figure S10 and Table S1. By comparing the snapshots of the DRIFTS peaks for the three catalysts, a sharp contrast is evident in terms of the relative abundance of the surface species. The intermediate species can be grouped[39] in terms of the intermediate oxidation species with non- or first C−C bond cleavage (e.g., ester, acetone, enolate, and acetate, i.e., Group-I) and those with the first and second C−C bond cleavage (e.g., bicarbonate, formate, monocarbonate, methoxy, i.e., Group II). The surface of PPN-3 is apparently enriched with acetone and enolate (Group-I) and bicarbonate and monocarbonate (Group II) species in much greater abundances than those on the other two catalysts. The surfaces of PPN-1 and PPN-2 appear to be enriched with ester and acetate (Group-I) and formate and methoxy (Group II) species.

While the exact reaction mechanisms for the catalytic oxidation cannot be derived from the current data, the sharp differences in terms of the surface intermediate species abundances likely reflect the subtle differences in surface/lattice oxygenation of the catalysts. For PPN-3, the first atomic PDF peak interatomic bond distance reaches a minimum 2.72 Å, suggesting that the Ni-enriched surface/subsurface layers are responsible for the surface oxygenation. The oxygenated species are highly active in reacting with propane to achieve the second C−C bond cleavage and C oxygenation. Thus, the first atomic PDF peak interatomic bond distance remains largely stable after the initial change. In contrast, the Ni-poor surface/subsurface layers for PPN-1 and PPN-2 show less activity in the surface oxygenation. The consequent slow oxygen transfer processes for the C−C bond cleavage and C oxygenation may be gradually developed over the entire NP, leading to a slow oscillatory behavior of the interatomic bond distance, as reflected by the first atomic PDF peak.

Mechanistically, the complete oxidation of propane follows two major steps, dehydrogenation of propane and oxygenation, forming oxy-carbon intermediate species toward CO_2.[60] The observation of the strong intensities of Group-I species with single oxygenation (e.g., acetone and enolate) and Group II species with triple oxygenation (e.g., bicarbonate and monocarbonate) seems to correlate well with the high catalytic activity over the catalyst with a higher Ni composition (>50% Ni), that is, PPN-3. The observation of the lower catalytic activities of the surface species for the catalysts with lower-Ni composition (<50% Ni), that is, PPN-1 and PPN-2, appear to reflect the Group-I species with double oxygenation (e.g., ester and acetate) and Group II species with single/double oxygenation (e.g., formate and methoxy). This is an intriguing finding, suggesting a correlation to the degree of C−C cleavage and oxygenation in the intermediate reaction steps. In comparison, the catalysts with a higher Ni composition (PPN-3) apparently favor less oxygenation (acetone and enolate) upon the first C−C bond cleavage followed by more oxygenation (bicarbonate and monocarbonate) upon the second C−C bond cleavage. This synergy, in combination with the rich Ni oxygenation sites on the surface/subsurface (PPN-3), likely contributed to the insignificant oscillation of the lattice strain during the reaction. The poor Ni oxygenation sites on the surface/subsurface of PPN-1 and PPN-2 favor more oxygenation (e.g., ester and acetate) upon the first C−C bond cleavage followed by less oxygenation (e.g., formate and methoxy) upon the second C−C bond cleavage, leading apparently to insufficient lattice oxygen supply and thus oscillatory behavior of the lattice strain. These subtle differences are illustrated in Figure 7IV by the proposed changes in surface oxygenation/deoxygenation and lattice strain of the catalysts containing lower-Ni% (PPN-1 and PPN-2) and higher-Ni% (PPN-3) under the propane oxidation condition.

Given this understanding, we further considered the propensity of oxygenation of Ni species in the alloy by the DFT calculation of the relative barriers for the surface diffusion of the oxygen species on different surface sites of the alloy. As shown in Figure 8, the oxygen adsorption energies and diffusion

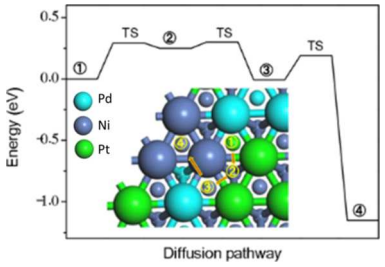

Figure 8. Calculated energies and energy barriers for the surface diffusion of oxygen species in different surface sites of the PtPdNi alloy.

energies show significant differences on different surface sites such as unary, binary, and ternary sites. The ternary Ni site features the lowest energy for binding O species, which is consistent with the highest oxophilicity. The results support qualitatively the assessment that the presence of Ni species near the Pt/Pd sites enables the propensity of O-activation, which aids the surface oxidation of propane on the Pt/Pd sites.

4. CONCLUSIONS

In summary, the ternary PtPdNi NPs supported on Al_2O_3 exhibit strong Ni-composition-dependent catalytic activity, showing a clear increase with Ni > 50%. The role of nanophase and surface structures of the catalysts is revealed by the combined HE-XRD/PDF and DRIFTS operando characterizations. The formation of different surface intermediates during the oxidation of propane is dominated by the favorability to less oxygenation of carbon upon the first C−C bond cleavage followed by more oxygenation of carbon upon the second C−C bond cleavage on the surface of ternary catalysts with Ni > 50%. This finding contrasts with the favorability to more oxygenation of carbon upon the first C−C bond cleavage followed by less oxygenation of carbon upon the second C−C bond cleavage on the surface of ternary catalysts with Ni < 50%. This catalytic synergy is further shown to correlate with the insignificant or slow lattice oscillations depending on the composition of the surface/subsurface Ni in the alloy. While the detailed structures of the active sites remain to be determined, the results suggest that Pt/Pd works as the active site for the C−H and C−C cleavage, while oxygenated Ni sites provide activated oxygen species for the oxygenation of the cleaved intermediates. This was supported by the comparison of the surface species based on DRIFTS data and also supported by the DFT calculation of the energy barriers for surface oxygen diffusion on the different surface sites. It is evident that the high oxyphilicity or high degree of oxygenation by the introduction of Ni into PtPd has

https://doi.org/10.1021/acsami.1c24007
ACS Appl. Mater. Interfaces 2022, 14, 11435−11447

played a significant role in maneuvering the activity of the oxygenated species over the catalyst's surface sites during propane oxidation, with both composition and structural effects on the C−C bond cleavage, oxygen activation, and carbon oxygenation. The surface/subsurface oxygenated metal sites play a crucial role in activating both O−O bond and C−C bond cleavages. Further understanding of quantitative relationship between the dynamic change of the atomic strain and the detailed surface reactivity, along with the XPS characterization of the surface state of the catalyst and the effect of the d-band center, will provide insights into the design of nanoalloy catalysts with fine-tunable catalytic activity and stability, which is part of our ongoing investigations.

■ ASSOCIATED CONTENT

Supporting Information

The Supporting Information is available free of charge at https://pubs.acs.org/doi/10.1021/acsami.1c24007.

Additional TEM/HRTEM images, HE-XRD/PDF patterns, DRIFTS, and activity data analyses (PDF)

■ AUTHOR INFORMATION

Corresponding Author

Chuan-Jian Zhong − *Department of Chemistry, State University of New York at Binghamton, Binghamton, New York 13902, United States;* orcid.org/0000-0003-0746-250X; Email: cjzhong@binghamton.edu

Authors

Haval Kareem − *Sensors and Electron Devices Directorate, CCDC Army Research Laboratory, Adelphi, Maryland 20783, United States; Department of Chemistry, State University of New York at Binghamton, Binghamton, New York 13902, United States*

Yazan Maswadeh − *Department of Physics, Central Michigan University, Mt. Pleasant, Michigan 48859, United States*

Zhi-Peng Wu − *Department of Chemistry, State University of New York at Binghamton, Binghamton, New York 13902, United States*

Asher C. Leff − *Sensors and Electron Devices Directorate, CCDC Army Research Laboratory, Adelphi, Maryland 20783, United States*

Han-Wen Cheng − *Laboratory of Advanced Materials, Department of Materials Science and Collaborative Innovation Center, Fudan University, Shanghai 200438, China*

Shiyao Shan − *Department of Chemistry, State University of New York at Binghamton, Binghamton, New York 13902, United States;* orcid.org/0000-0001-9240-7227

Shan Wang − *Department of Chemistry, State University of New York at Binghamton, Binghamton, New York 13902, United States*

Richard Robinson − *Department of Chemistry, State University of New York at Binghamton, Binghamton, New York 13902, United States*

Dominic Caracciolo − *Department of Chemistry, State University of New York at Binghamton, Binghamton, New York 13902, United States*

Alex Langrock − *Sensors and Electron Devices Directorate, CCDC Army Research Laboratory, Adelphi, Maryland 20783, United States*

David M. Mackie − *Sensors and Electron Devices Directorate, CCDC Army Research Laboratory, Adelphi, Maryland 20783, United States*

Dat T. Tran − *Sensors and Electron Devices Directorate, CCDC Army Research Laboratory, Adelphi, Maryland 20783, United States*

Valeri Petkov − *Department of Physics, Central Michigan University, Mt. Pleasant, Michigan 48859, United States;* orcid.org/0000-0002-6392-7589

Complete contact information is available at: https://pubs.acs.org/10.1021/acsami.1c24007

Notes

The authors declare no competing financial interest.

■ ACKNOWLEDGMENTS

This work was supported by the National Science Foundation (CHE 2102482 and 1566283) and the Department of Energy—Basic Energy Sciences (DE-SC0006877). Work and access to Beamline 11-ID-B at the Advanced Photon Source was supported by the U.S. Department of Energy (DOE) Office of Science under Contract DE-AC02-06CH11357. Partial support of SUNY TAF funding is also acknowledged. K. Beyer's help with the in situ DRIFTS experiments is also acknowledged. Support of FEVERAM funding for H.K. and D.M. is also acknowledged.

■ REFERENCES

(1) Zhang, W.; Díez-Ramírez, J.; Anguita, P.; Descorme, C.; Valverde, J. L.; Giroir-Fendler, A. Nanocrystalline Co_3O_4 Catalysts for Toluene and Propane Oxidation: Effect of The Precipitation Agent. *Appl. Catal., B* **2020**, *273*, No. 118894.

(2) Sahoo, B.; Sahoo, N.; Saha, U. Effect of engine parameters and type of gaseous fuel on the performance of dual-fuel gas diesel engines—A critical Review. *Renew. Sustainable Energy Rev.* **2009**, *13*, 1151−1184.

(3) Enterkin, J. A.; Setthapun, W.; Elam, J. W.; Christensen, S. T.; Rabuffetti, F. A.; Marks, L. D.; Stair, P. C.; Poeppelmeier, K. R.; Marshall, C. L. Propane Oxidation Over Pt/Srtio3 Nanocuboids. *ACS Catal.* **2011**, *1*, 629−635.

(4) Werpy, M. R.; Burnham, A.; Bertram, K. Illinois, USA: Center for Transportation Research, Argonne National Laboratory, 2010. https://publications.anl.gov/anlpubs/2010/06/67243.pdf (accessed October 20, 2021).

(5) Stambouli, A. B. Fuel cells: The Expectations for An Environmental-Friendly and Sustainable Source of Energy. *Renew. Sustainable Energy Rev.* **2011**, *15*, 4507−4520.

(6) Yarime, M. Public Coordination for Escaping from Technological Lock-In: Its Possibilities and Limits in Replacing Diesel Vehicles with Compressed Natural Gas Vehicles in Tokyo. *J. Cleaner Prod.* **2009**, *17*, 1281−1288.

(7) Li, Y.; Wang, X.; Xie, C.; Song, C. Influence of Ceria and Nickel Addition to Alumina-Supported Rh Catalyst for Propane Steam Reforming at Low Temperatures. *Appl. Catal., A* **2009**, *357*, 213−222.

(8) Beer, T.; Grant, T.; Williams, D.; Watson, H. Fuel-Cycle Greenhouse Gas Emissions from Alternative Fuels in Australian Heavy Vehicles. *Atmos. Environ.* **2002**, *36*, 753−763.

(9) Peter, C.; Derible, A.; Parmentier, J.; Le Drian, C.; Becht, J.-M. A Green Direct Preparation of a Magnetic Ordered Mesoporous Carbon Catalyst Containing Fe−Pd Alloys: Application to Suzuki−Miyaura Reactions in Propane-1,2-dio. *New J. Chem.* **2017**, *41*, 4931−4936.

(10) Wan Hussin, D.; Traa, Y. Production of High-Octane Fuel Components by Dehydroalkylation of Benzene with Mixtures of Ethane and Propane. *Energy Fuel* **2014**, *28*, 3352−3356.

(11) Zhang, H.; Li, C.; Lu, Q.; Cheng, M.-J.; Goddard, W. A., III Selective Activation of Propane Using Intermediates Generated during Water Oxidation. *J. Am. Chem. Soc.* **2021**, *143*, 3967−3974.
(12) Liu, Y.-R.; Li, X.; Liao, W.-M.; Jia, A.-P.; Wang, Y.-J.; Luo, M.-F.; Lu, J.-Q. Highly Active Pt/Bn Catalysts for Propane Combustion: The Roles of Support and Reactant-Induced Evolution of Active Sites. *ACS Catal.* **2019**, *9*, 1472−1481.
(13) Kim, J.; Abbott, M. S.; Go, D. B.; Hicks, J. C. Enhancing C−H Bond Activation of Methane Via Temperature-Controlled, Catalyst−Plasma Interactions. *ACS Energy Lett.* **2016**, *1*, 94−99.
(14) Kathiraser, Y.; Oemar, U.; Saw, E. T.; Li, Z.; Kawi, S. Kinetic and Mechanistic Aspects for Co_2 Reforming of Methane Over Ni Based Catalysts. *Chem. Eng. J.* **2015**, *278*, 62−78.
(15) Chaar, M.; Patel, D.; Kung, H. H. Selective Oxidative Dehydrogenation of Propane Over V—Mg—O Catalysts. *J. Catal.* **1988**, *109*, 463−467.
(16) Caplain, I.; Cazier, F.; Nouali, H.; Mercier, A.; Déchaux, J.-C.; Nollet, V.; Joumard, R.; André, J.-M.; Vidon, R. Emissions of Unregulated Pollutants from European Gasoline and Diesel Passenger Cars. *Atmos. Environ.* **2006**, *40*, 5954−5966.
(17) Wang, A.; Olsson, L. The Impact of Automotive Catalysis on The United Nations Sustainable Development Goals. *Nat. Catal.* **2019**, *2*, 566−570.
(18) Farrauto, R. J.; Deeba, M.; Alerasool, S. Gasoline Automobile Catalysis and Its Historical Journey to Cleaner Air. *Nat. Catal.* **2019**, *2*, 603−613.
(19) Datye, A. K.; Votsmeier, M. Opportunities and Challenges in the Development of Advanced Materials for Emission Control Catalysts. *Nat. Mater.* **2020**, *20*, 1049.
(20) Ren, Z.; Wu, Z.; Song, W.; Xiao, W.; Guo, Y.; Ding, J.; Suib, S. L.; Gao, P.-X. Low Temperature Propane Oxidation Over Co3o4 Based Nano-Array Catalysts: Ni Dopant Effect, Reaction Mechanism and Structural Stability. *Appl. Catal., B* **2016**, *180*, 150−160.
(21) Luo, J.-Y.; Meng, M.; Yao, J.-S.; Li, X.-G.; Zha, Y.-Q.; Wang, X.; Zhang, T.-Y. One-Step Synthesis of Nanostructured Pd-Doped Mixed Oxides Mox-Ceo2 (M = Mn, Fe, Co, Ni, Cu) For Efficient Co and C_3H_8 Total Oxidation. *Appl. Catal., B* **2009**, *87*, 92−103.
(22) Baldi, M.; Finocchio, E.; Milella, F.; Busca, G. Catalytic Combustion of C_3 Hydrocarbons and Oxygenates over mn3o4. *Appl. Catal., B* **1998**, *16*, 43−51.
(23) Liu, H.; Song, C.; Zhang, L.; Zhang, J.; Wang, H.; Wilkinson, D. P. A Review of Anode Catalysis in The Direct Methanol Fuel Cell. *J. Power Sources* **2006**, *155*, 95−110.
(24) Papageorgopoulos, D.; Keijzer, M.; Veldhuis, J.; De Bruijn, F. Co Tolerance of Pd-Rich Platinum Palladium Carbon-Supported Electrocatalysts: Proton Exchange Membrane Fuel Cell Applications. *J. Electrochem. Soc.* **2002**, *149*, A1400.
(25) Wu, J.; Shan, S.; Cronk, H.; Chang, F.; Kareem, H.; Zhao, Y.; Luo, J.; Petkov, V.; Zhong, C. J. Understanding Composition-Dependent Synergy of PtPd Alloy Nanoparticles in Electrocatalytic Oxygen Reduction Reaction. *J. Phys. Chem. C* **2017**, *121*, 14128−14136.
(26) Eid, K.; Sliem, M. H.; Abdullah, A. M. Unraveling Template-Free Fabrication of Carbon Nitride Nanorods Cooped with Pt and Pd for Efficient Electrochemical and Photoelectrochemical Carbon Monoxide Oxidation at Room Temperature. *Nanoscale* **2019**, *11*, 11755−11764.
(27) Xiong, H.; Wiebenga, M. H.; Carrillo, C.; Gaudet, J. R.; Pham, H. N.; Kunwar, D.; Oh, S. H.; Qi, G.; Kim, C. H.; Datye, A. K. Design Considerations for Low-Temperature Hydrocarbon Oxidation Reactions on Pd Based Catalysts. *Appl. Catal., B* **2018**, *236*, 436−444.
(28) Shan, S.; Petkov, V.; Yang, L.; Luo, J.; Joseph, P.; Mayzel, D.; Prasai, B.; Wang, L.; Engelhard, M.; Zhong, C. J. Atomic-Structural Synergy for Catalytic Co Oxidation Over Palladium−Nickel Nanoalloys. *J. Am. Chem. Soc.* **2014**, *136*, 7140−7151.
(29) Yang, L.; Shan, S.; Loukrakpam, R.; Petkov, V.; Ren, Y.; Wanjala, B. N.; Engelhard, M. H.; Luo, J.; Yin, J.; Chen, Y.; Zhong, C. J. Role of Support−Nanoalloy Interactions in The Atomic-Scale Structural and Chemical Ordering for Tuning Catalytic Sites. *J. Am. Chem. Soc.* **2012**, *134*, 15048−15060.
(30) Wu, Z. P.; Caracciolo, D. T.; Maswadeh, Y.; Wen, J.; Kong, Z.; Shan, S.; Vargas, J. A.; Yan, S.; Hopkins, E.; Park, K.; Sharma, A.; Ren, Y.; Petkov, V.; Wang, L.; Zhong, C. J. Alloying−Realloying Enabled High Durability for Pt−Pd-3d-Transition Metal Nanoparticle Fuel Cell Catalysts. *Nat. Commun.* **2021**, *12*, 859.
(31) Chen, C.; Kang, Y.; Huo, Z.; Zhu, Z.; Huang, W.; Xin, H. L.; Snyder, J. D.; Li, D.; Herron, J. A.; Mavrikakis, M.; Chi, M.; More, K. L.; Li, Y.; Markovic, N. M.; Somorjai, G. A.; Yang, P. D.; Stamenkovic, V. R. Highly Crystalline Multimetallic Nanoframes with Three-Dimensional Electrocatalytic Surfaces. *Science* **2014**, *343*, 1339−1343.
(32) Wang, Q.; Zhao, Q.; Su, Y.; Zhang, G.; Xu, G.; Li, Y.; Liu, B.; Zheng, D.; Zhang, J. Hierarchical Carbon and Nitrogen Adsorbed PtNiCo Nanocomposites with Multiple Active Sites for Oxygen Reduction and Methanol Oxidation Reactions. *J. Mater. Chem. A* **2016**, *4*, 12296−12307.
(33) Wu, Z. P.; Shan, S.; Zang, S. Q.; Zhong, C. J. Dynamic Core−Shell and Alloy Structures of Multimetallic Nanomaterials and Their Catalytic Synergies. *Acc. Chem. Res.* **2020**, *53*, 2913−2924.
(34) Kong, Z.; Maswadeh, Y.; Vargas, J. A.; Shan, S.; Wu, Z. P.; Kareem, H.; Leff, A. C.; Tran, D. T.; Chang, F.; Yan, S.; Nam, S.; Zhao, X.; Lee, J. M.; Luo, J.; Shastri, S.; Yu, G.; Petkov, V.; Zhong, C. J. Origin of High Activity and Durability of Twisty Nanowire Alloy Catalysts Under Oxygen Reduction and Fuel Cell Operating Conditions. *J. Am. Chem. Soc.* **2019**, *142*, 1287−1299.
(35) Petkov, V.; Prasai, B.; Shastri, S.; Kim, J.-W.; Shan, S.; Kareem, H. R.; Luo, J.; Zhong, C. J. Surface Atomic Structure and Functionality of Metallic Nanoparticles: A Case Study of Au−Pd Nanoalloy Catalysts. *J. Phys. Chem. C* **2017**, *121*, 7854−7866.
(36) Shan, S.; Li, J.; Maswadeh, Y.; O'Brien, C.; Kareem, H.; Tran, D. T.; Lee, I. C.; Wu, Z. P.; Wang, S.; Yan, S.; Cronk, H.; Mott, D.; Yang, L.; Luo, J.; Petkov, V.; Zhong, C. J. Surface Oxygenation of Multicomponent Nanoparticles Toward Active and Stable Oxidation Catalysts. *Nat. Commun.* **2020**, *11*, 1−9.
(37) Petkov, V.; Maswadeh, Y.; Lu, A.; Shan, S.; Kareem, H.; Zhao, Y.; Luo, J.; Zhong, C. J.; Beyer, K.; Chapman, K. Evolution of Active Sites in Pt-Based Nanoalloy Catalysts for the Oxidation of Carbonaceous Species by Combined in Situ Infrared Spectroscopy and Total X-ray Scattering. *ACS Appl. Mater. Interfaces* **2018**, *10*, 10870−10881.
(38) Kareem, H.; Shan, S.; Lin, F.; Li, J.; Wu, Z.; Prasai, B.; O'Brien, C. P.; Lee, I. C.; Tran, D. T.; Yang, L.; Mott, D.; Luo, J.; Petkov, V.; Zhong, C. J. Evolution of Surface Catalytic Sites on Thermochemically-Tuned Gold−Palladium Nanoalloys. *Nanoscale* **2018**, *10*, 3849−3862.
(39) Kareem, H.; Shan, S.; Wu, Z. P.; Velasco, L.; Moseman, K.; O'Brien, C. P.; Tran, D. T.; Lee, I. C.; Maswadeh, Y.; Yang, L.; Mott, D.; Luo, J.; Petkov, V.; Zhong, C. J. Catalytic Oxidation of Propane Over Palladium Alloyed with Gold: An Assessment of The Chemical and Intermediate Species. *Catal. Sci. Technol.* **2018**, *8*, 6228−6240.
(40) Beyer, K. A.; Zhao, H.; Borkiewicz, O. J.; Newton, M. A.; Chupas, P. J.; Chapman, K. W. Simultaneous Diffuse Reflection Infrared Spectroscopy and X-Ray Pair Distribution Function Measurements. *J. Appl. Crystallogr.* **2014**, *47*, 95−101.
(41) Fang, R.; Cui, Y.; Shi, Z.; Gong, M.; Chen, Y. Promotion of A Pd/Al2o3 Close-Coupled Catalyst by Ni. *Chin. J. Catal.* **2015**, *36*, 994−1000.
(42) Li, Y.; Wang, X.; Song, C. Spectroscopic Characterization and Catalytic Activity of Rh Supported on Ceo2-Modified Al2o3 for Low-Temperature Steam Reforming of Propane. *Catal. Today* **2016**, *263*, 22−34.
(43) Wanjala, B. N.; Loukrakpam, R.; Luo, J.; Njoki, P. N.; Mott, D.; Zhong, C.-J.; Shao, M.; Protsailo, L.; Kawamura, T. Thermal Treatment of Ptnico Electrocatalysts: Effects of Nanoscale Strain and Structure on The Activity and Stability for The Oxygen Reduction Reaction. *J. Phys. Chem. C* **2010**, *114*, 17580−17590.
(44) Lu, Y.; Jiang, Y.; Chen, W. Graphene Nanosheet-Tailored PtPd Concave Nanocubes with Enhanced Electrocatalytic Activity and Durability for Methanol Oxidation. *Nanoscale* **2014**, *6*, 3309−3315.
(45) Li, M.; Wu, X.; Liu, S.; Wan, J.; Ran, R.; Weng, D. Effects of Baria on Propane Oxidation Activity of Pd/Al2o3 Catalyst: Pd−Bao Interaction and Reaction Routes. *Prog. Nat. Sci.* **2014**, *24*, 280−286.

(46) Wu, X.; Zhang, L.; Weng, D.; Liu, S.; Si, Z.; Fan, J. Total Oxidation of Propane on Pt/Wox/Al2o3 Catalysts by Formation of Metastable Ptδ+ Species Interacted with Wox Clusters. *J. Hazard. Mater.* **2012**, *225*, 146−154.
(47) Petkov, V.; Maswadeh, Y.; Vargas, J. A.; Shan, S.; Kareem, H.; Wu, Z. P.; Luo, J.; Zhong, C. J.; Shastri, S.; Kenesei, P. Deviations from Vegard's Law and Evolution of The Electrocatalytic Activity and Stability of Pt-Based Nanoalloys Inside Fuel Cells by In Operando X-ray Spectroscopy and Total Scattering. *Nanoscale* **2019**, *11*, 5512−5525.
(48) Faria, W. L.; Perez, C. A.; César, D. V.; Dieguez, L. C.; Schmal, M. In Situ Characterizations of Pd/Al2o3 and Pd/Ceo2/Al2o3 Catalysts for Oxidative Steam Reforming of Propane. *Appl. Catal., B* **2009**, *92*, 217−224.
(49) Schubert, M. M.; Gasteiger, H. A.; Behm, R. J. Surface Formates as Side Products in The Selective Co Oxidation on Pt/γ-Al2O3. *J. Catal.* **1997**, *172*, 256−258.
(50) He, H.; Yu, Y. Selective Catalytic Reduction of NOx Over Ag/Al2o3 Catalyst: From Reaction Mechanism to Diesel Engine Test. *Catal. Today* **2005**, *100*, 37−47.
(51) Van den Brand, J.; Blajiev, O.; Beentjes, P.; Terryn, H.; De Wit, J. Interaction of Ester Functional Groups with Aluminum Oxide Surfaces Studied Using Infrared Reflection Absorption Spectroscopy. *Langmuir* **2004**, *20*, 6318−6326.
(52) Yigezu, Z. D.; Muthukumar, K. Structural Characteristics of Selected Metal Oxides Used for The Catalytic Pyrolysis of Sunflower Oil. *J. Anal. Appl. Pyrolysis* **2015**, *114*, 60−67.
(53) Anbarasan, R.; Dhanalakshmi, V. Melt Functionalization of Ldpe with Thio Ester, Amino Ester, And Hydroxy Ester by Thermolysis Method—An FTIR Study. *J. Appl. Polym. Sci.* **2011**, *122*, 2252−2261.
(54) Rethwisch, D. G.; Dumesic, J. Effect of metal-oxygen bond strength on properties of oxides. 1. Infrared spectroscopy of adsorbed carbon monoxide and carbon dioxide. *Langmuir* **1986**, *2*, 73−79.
(55) Morterra, C.; Magnacca, G. A case study: Surface Chemistry and Surface Structure of Catalytic Aluminas, As Studied by Vibrational Spectroscopy of Adsorbed Species. *Catal. Today* **1996**, *27*, 497−532.
(56) Wan, J.; Ran, R.; Li, M.; Wu, X.; Weng, D. Effect of Acid and Base Modification on The Catalytic Activity of Pt/Al_2o_3 for Propene Oxidation. *J. Mol. Catal. A: Chem.* **2014**, *383*, 194−202.
(57) Yu, Y.; He, H.; Feng, Q.; Gao, H.; Yang, X. Mechanism of The Selective Catalytic Reduction of NO*x* by C_2H_5OH over Ag/Al_2O_3. *Appl. Catal., B* **2004**, *49*, 159−171.
(58) McInroy, A. R.; Lundie, D. T.; Winfield, J. M.; Dudman, C. C.; Jones, P.; Lennon, D. The Application of Diffuse Reflectance Infrared Spectroscopy and Temperature-Programmed Desorption to Investigate the Interaction of Methanol On H-Alumina. *Langmuir* **2005**, *21*, 11092−11098.
(59) Ozensoy, E.; Herling, D.; Szanyi, J. Nox Reduction on A Transition Metal-Free Γ-Al_2O_3 Catalyst Using Dimethyl ether (DME). *Catal. Today* **2008**, *136*, 46−54.
(60) Li, G.; Li, N.; Sun, Y.; Qu, Y.; Jiang, Z.; Zhao, Z.; Zhang, Z.; Cheng, J.; Hao, Z. Efficient Defect Engineering in Co-Mn Binary Oxides for Low-Temperature Propane Oxidation. *Appl. Catal., B* **2021**, *282*, No. 119512.

https://doi.org/10.1021/acsami.1c24007
ACS Appl. Mater. Interfaces 2022, 14, 11435−11447